Supplementary Information: Localizing and Tracking Single Nanoscale Emitters in Three Dimensions with High Spatio-Temporal Resolution Using a Double-Helix Point Spread Function

Michael A. Thompson[1]*, Matthew D. Lew[2]*, Majid Badieirostami[1], and W. E. Moerner[1]
Departments of [1]Chemistry and [2]Electrical Engineering, Stanford University, Stanford, CA 94305
(*Equal contributions)

A. Setup Collection Efficiency

In the setup implemented in this paper, there are two major sources of photon collection inefficiency. Since the liquid crystals in the SLM can only modulate one polarization, a linear polarizer is used to reject the unmodulated beam. In principle, this rejected light could be collected and also modulated, but for experimental simplicity in these experiments we chose to only use one polarization. The efficiency of our linear polarizer in passing aligned polarized light is quite good, measured at 44%.

A more fundamental loss comes from the phase mask and the SLM. The reflectivity of the SLM is uniform at about 92% for wavelengths of 500-700 nm, which is very high as a result of the use of a built-in dielectric mirror behind the liquid crystal layer. Also, the SLM modulates effectively the entire vertically polarized incident light beam due to a high effective fill fraction, quoted at 95%. The main loss comes from the inefficiency of the phase mask in directing the photons into the two main lobes which are used for fitting. Of course, if we fit to the actual extended DH-PSF instead of two Gaussians these photons would not be lost, rather they would be used to gain more information about the location of the molecule. To calculate the overall efficiency, 40 nm fluorescent beads (Invitrogen) emitting at 580 nm pumped with a 561 nm

diode laser were imaged with the polarizer taken out and the phase mask on the SLM turned off which was compared to the photon counts in the two lobes of the DH-PSF with the phase mask on and the polarizer in place. The efficiency was found to be ~35% for photons arriving in a 3 micron area. This efficiency is very sensitive to the alignment of the setup and the wavelength of the emission. The efficiency of the system also depends on the z position of the emitter. However, as noted above, 44% of this 35% overall efficiency could be recovered if both polarizations are modulated and imaged. Therefore, improving the efficiency of the system is possible with simple modifications and will be the subject of future study.

B. Theoretical Model of Experimental Setup

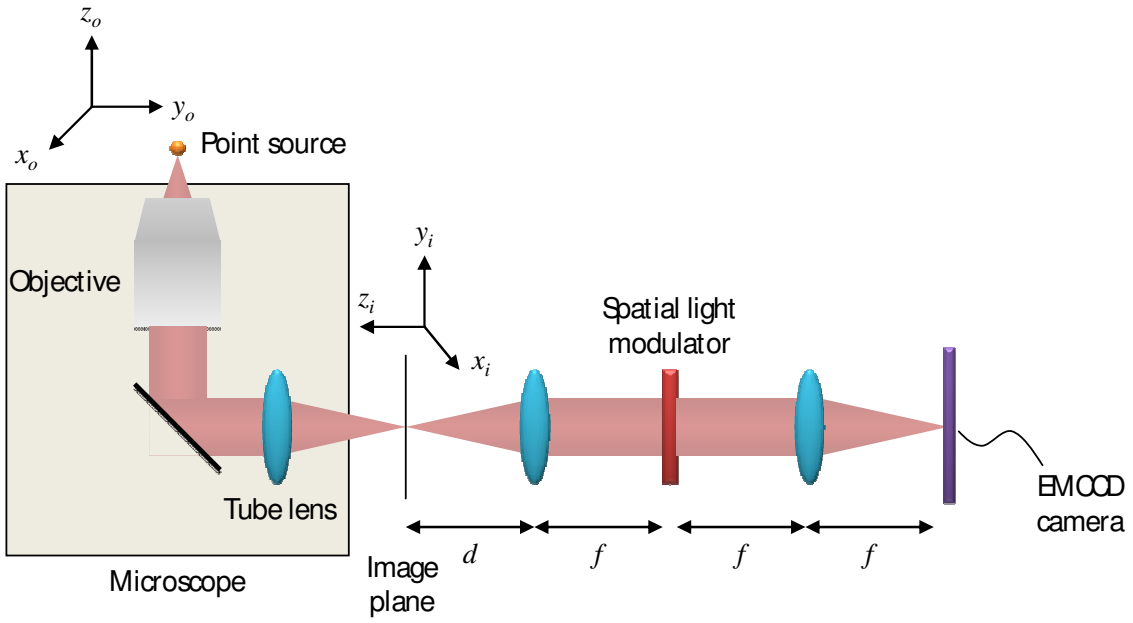

Figure S1. Schematic showing the essential components of our DH-PSF setup and relevant parameters.

A computational model of the microscope and 4*f* imaging system is necessary for calculating the Fisher information of the DH-PSF. Specifically, the image of the DH-PSF as measured by the EMCCD camera must be calculated as a function of the location of a point

source in the sample volume of the objective lens (see Figure S1). The microscope maps the location of the point source in the object plane, (x_o, y_o, z_o), to a location in the image plane, (x_i, y_i, z_i), which is given by

$$\begin{aligned} x_i &= Mx_o \\ y_i &= My_o \\ z_i &= n_{oil} M^2 z_o = f - d \end{aligned},$$

where $z_o = 0$ defines the focal plane of the objective lens, $d = f - z_i$ gives the distance between the point source image and the first lens in the 4*f* system, *M* is the magnification of the objective lens, and n_{oil} is the index of refraction of the immersion oil. The index of refraction of the immersion oil must be taken into account since the sample is immersed in oil, while the image of the sample is formed in air.

Once the location of the image of the point source is determined, it is relatively straightforward to calculate the image of the DH-PSF on the EMCCD camera. Assuming that the numerical aperture of the system is sufficiently large, the Fourier transform of the point source in the image plane is a uniform intensity distribution at the spatial light modulator. This distribution is modulated by the phase mask of the spatial light modulator, which is then Fourier transformed onto the EMCCD camera. Thus, the image of the DH-PSF, $U(u,v)$, is given by[1]

$$U(u,v) = \left| \frac{1}{i\lambda f} \exp\left[i \frac{\pi z_i}{\lambda f^2} \left((u - x_i)^2 + (v - y_i)^2 \right) \right] \Im\left\{ t_A\left(\frac{u - x_i}{\lambda f}, \frac{v - y_i}{\lambda f} \right) \right\} \right|^2 ,$$

where λ is the wavelength of the point emitter, *f* is the focal length of the lenses in the 4*f* system, (x_i, y_i, z_i) is the location of the point source image in the image plane, (u,v) are coordinates on the EMCCD camera, $\Im$ is the two-dimensional Fourier transform operator, and $t_A(x,y)$ is the transmittance function of the phase mask. It is important to note that this model assumes a

coherent monochromatic point emitter. This assumption is largely for computational speed and convenience, and we find that this model predicts the behavior of the DH-PSF with reasonable accuracy.

C. Fisher Information Calculations

The position estimation accuracy of a PSF is quantified by its Fisher information content. The inverse of the Fisher information is called the Cramer-Rao bound (CRB) which is the lowest possible position estimation variance that can be achieved by an unbiased estimator based on that PSF, i.e., $\sigma^2 \geq \mathbf{I}^{-1}(\theta)$. The square root of the CRB is the limit of the localization accuracy which is provided in the paper in Figure 2D at z = 0 as a function of the number of photons and in Figure 3C as a function of the axial position of the emitter, z.

In order to calculate the limit of the localization accuracy we have adopted the same methodology described previously[2, 3] with the only difference that the image function, i.e. $q_{z_0}(x, y)$, is replaced by the DH-PSF shown in Figure S2. For a pixelated detector with additive Poisson noise with mean β per pixel, the Fisher information matrix is calculated as follows:

$$\mathbf{I}(\theta) = \sum_{k=1}^{N_p} \frac{1}{\mu_\theta(k) + \beta} \left(\frac{\partial \mu_\theta(k)}{\partial \theta} \right)^T \frac{\partial \mu_\theta(k)}{\partial \theta} \qquad \theta = (x_0, y_0, z_0) \in \Theta$$

where $\mu_\theta(k) = N \int_{C_k} \frac{1}{M^2} q_{z_0}\left(\frac{x}{M} - x_0, \frac{y}{M} - y_0 \right) dxdy$. Here Θ denotes the parameter space, N_p denotes the number of pixels, N denotes the number of photons, C_k is the region in the xy-plane occupied by the kth pixel, M denotes the lateral magnification of the microscope, (x_0, y_0, z_0)

denotes the 3D location of the single molecule in the object space, and the q_{z_0} denotes the image function of a single molecule.

In our calculation we have used $M = 100$, $N_p = 625$ pixels (i.e., array of 25 × 25 pixels) with square pixels of width 160 nm, and additive Poisson noise whose mean scales linearly with the photons present in the DH-PSF. Although we used the natural heterogeneity in brightness of different beads to provide different numbers of detected photons in our experiments, we chose this linear scaling of the additive noise in our simulations to mimic the effect of weak tails of the DH-PSF acting as a brightness-dependent background signal. While an optimal estimator would be able to take any weak tails into account, these tails appear as additional background to the double-Gaussian fitting algorithm. The additive Poisson noise has a mean value of $\beta = 2$ photons/pixel for 1000 photons present in the DH-PSF, which closely matches our experimental setup for the case of Figs. 2C and 3B. The other noise sources are negligible and they are not included in our calculation. It is noteworthy that unlike the standard PSF there is no closed-form formula for the DH-PSF, therefore all our results are numerically calculated from the 3D sampled function in Figure S2, which was computed from the DH-PSF phase mask using the model described above.

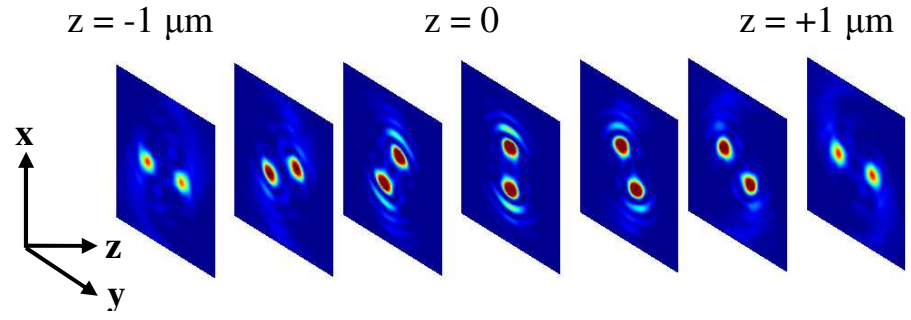

Figure S2. The numerically obtained DH-PSF images versus axial distance for λ = 633 nm which is used as the image function $q_{z_0}(x, y)$ in the Fisher information calculation.

D. Calibration of CCD Gain for Photon Counting

In order to convert EMCCD camera ADC counts to detected photons, two calibrations are required: the conversion gain, (number of e^- after on-chip gain)/(ADC count), and the electron multiplication gain (number of e^- after on-chip gain)/(number of photoelectrons). The conversion gain was calibrated according to a previously published procedure [4]. Multiple images of a dim, uniform field are acquired (in this case, a blank, clean coverslip) for an arbitrary number of evenly spaced intensities with no EM gain. Due to the shot noise in the signal, a plot of the variance of the image for each intensity level versus the mean signal of the image for each intensity level should be a straight line with a slope that equals the inverse of the conversion gain. Pixel-to-pixel nonuniformity causes nonlinear effects that can be removed by taking two images at each intensity according to reference [4]. The conversion gain on our camera was found to be 24.7 electrons/count.

The Andor Ixon$^+$ used in these experiments has been calibrated such that the measured electron multiplication gain should be very similar to the software setting, but because this study forces us to know the photon counts very accurately, we calibrated the true gain as a function of the software gain. We measured the ratio of the mean signal under an arbitrary irradiance and the mean signal with the gain off (unity gain). A true EM gain of 305 was found for software settings of 300. To calculate the number of photons, we simply multiply the number of counts found from the molecule by the conversion gain of 24.7 electrons/count and divide by the electron multiplication gain of 305 to give photons detected.

E. Removal of Drift at High Photon Counts

Since all imaging systems have nonzero thermal and mechanical fluctuations, the noise from these fluctuations dominates any localization measurement in which the photon shot noise is low. For high numbers of photons (>1500), noise resulting from stage drift artificially inflates measurements of the localization precision of the DH-PSF. This is readily apparent by comparing the localization precision versus photons detected plots before (Figure S3(a)) and after (Figure S3(b)) removing drift noise from the measurements.

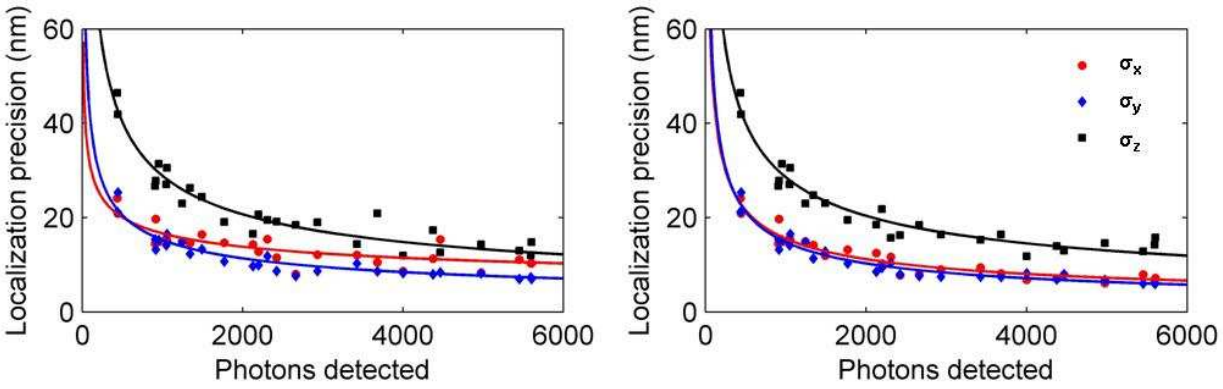

Figure S3. Plots of the localization precision versus the number of photons detected (a) before removing drift noise and (b) after removing drift noise. Both plots show photon counts ranging from 400-5500 photons. All three dimensions are plotted on the curve.

Each data point above was calculated by localizing a fluorescent bead 50 times and analyzing the statistics of these localizations. In the absence of noise, each of these localizations should give an identical location for the fluorescent bead. Fifty-frame datasets were collected; each frame of which contained images of multiple beads within the microscope's field of view. The brightest three beads within the dataset were used to characterize the stage drift within that dataset. The deviation of the location of each bead was calculated, relative to each bead's mean location for the entire dataset, as a function of frame number. These deviations were averaged over the three beads for each frame, and this average was taken as a measure of the stage drift over the fifty-frame dataset. The x, y, and z components of this stage drift were then subtracted from the measured locations of the other beads for each frame in the dataset, and these new

locations were used for calculating the localization precision shown in Figure S3(b). Note that the removal of drift noise from the localization measurements decreases the noise in the localization curves over different numbers of photons. It also decreases the localization precision measured for high numbers of photons, which is to be expected since one component of uncertainty has been removed from the data.

1. Goodman, J. W. *Introduction to Fourier Optics;* Roberts & Company Publishers: Greenwood Village, CO, 2005; , pp 491.

2. Ram, S.; Prabhat, P.; Chao, J.; Ward, E. S.; Ober, R. J. *Biophys. J.* **2008**, 6025-6043.

3. Ober, R. J.; Ram, S.; Ward, E. S. *Biophys. J.* **2004**, 1185-1200.

4. Newberry, M. Mirametrics Technical Note on Pixel Response Effects in CCD Camera Gain Calibration http://www.mirametrics.com/tech_note_ccdgain.htm.